

Transient Membrane Localization of SPV-1 Drives Cyclical Actomyosin Contractions in the *C. elegans* Spermatheca

Pei Yi Tan¹ and Ronen Zaidel-Bar^{1,2,*}¹Mechanobiology Institute, National University of Singapore, Singapore 117411, Singapore²Department of Biomedical Engineering, National University of Singapore, Singapore 117575, Singapore

Summary

Background: Actomyosin contractility is the major cellular force driving changes in cell and tissue shape. A principal regulator of contractility is the small GTPase RhoA. External mechanical forces have been shown to impact RhoA activity and cellular contractility. However, the mechanotransduction pathway from external forces to actomyosin contractility is poorly understood.

Results: Here, we show that actomyosin contractility in the *C. elegans* spermatheca is under control of RHO-1/RhoA, which, in turn, is regulated by the F-BAR and RhoGAP protein SPV-1. In the relaxed spermatheca, SPV-1 localizes through its F-BAR domain to the apical membrane, where it inhibits RHO-1/RhoA activity through its RhoGAP domain. Oocyte entry forces the spermatheca cells to stretch, and subsequently SPV-1 detaches from the membrane, permitting RHO-1 activity to increase. The increase in RHO-1 activity facilitates spermatheca contraction and expulsion of the newly fertilized embryo into the uterus, leading to relaxation of the spermatheca, SPV-1 membrane localization, and initiation of a new cycle.

Conclusions: Our results demonstrate how transient membrane localization of a novel F-BAR domain, likely via specific binding to curved membranes, coupled to a RhoGAP domain, can provide feedback between a mechanical signal (membrane stretching) and actomyosin contractility. We anticipate this to be a widely utilized feedback mechanism used to balance actomyosin forces in the face of externally applied forces, as well as intrinsic processes involving cell deformation, from single-cell migration to tissue morphogenesis.

Introduction

Actomyosin-mediated contractility is a universal mechanism for producing force in both muscle and nonmuscle cells. Coarrangements of actin and myosin work in concert to mediate important cellular processes, including cytokinesis, cell migration, and morphogenesis. Importantly, several lines of evidence suggest that external forces can modulate internal contractility. For example, smooth muscle cells that form the airway and endothelium have been documented to regulate their contractile behavior in response to cyclical stress resulting from breathing and blood flow, respectively [1–4]. At the molecular level, mechanical forces from external perturbations, such as shear, compressive, or tensile stress, have been shown to modulate contractility through the regulation of RhoA activity [2, 5].

The small GTPase RhoA is a well-established regulator of actomyosin contractility functioning primarily through two downstream effectors: the diaphanous-related formin (Dia1) and the Rho-associated serine/threonine kinase (ROCK) [6, 7]. Activated Dia1 is involved in the nucleation and elongation of actin filaments [6], whereas ROCK promotes myosin activation through phosphorylation of myosin light-chain (MLC) and myosin light-chain phosphatase (MLCP) [8, 9].

Although the downstream effectors of RhoA are well characterized, the transduction pathways through which mechanical stimuli lead to RhoA activation are far less understood. RhoA is activated by guanine nucleotide exchange factors (RhoGEFs), which facilitate the exchange of GDP for GTP [10], and is switched off by hydrolysis of GTP to GDP, a process greatly enhanced by GTPase activating proteins (RhoGAPs) [11]. Guanine nucleotide dissociation inhibitors (GDIs) function to bind and maintain the inactive pool of RhoA in the cytosol [12], whereas active RhoA localizes to the plasma membrane [13–15]. Thus, the spatiotemporal regulation of RhoA depends on the spatiotemporal localization of RhoGAPs and/or RhoGEFs. Indeed, tensional forces applied to integrins induce activation of RhoA through the recruitment of the RhoGEFs GEF-H1 and LARG to focal adhesions [16]. However, it is unclear by what mechanism RhoGEFs and RhoGAPs can change their localization in response to external forces.

Current understanding of how external forces lead to RhoA-mediated contractile events is primarily derived from in vitro cell-based studies [5]. Here, we propose a system in which mechanical regulation of RhoA activity in an epithelial tube can be investigated in vivo. During *C. elegans* ovulation, an oocyte is released into the spermatheca, an accordion-like myoepithelial pouch composed of 24 cells, which houses the sperm [17, 18]. Fertilization takes place in the spermatheca immediately upon oocyte entry, and orchestrated constriction of the spermatheca subsequently propels the fertilized embryo into the uterus. The spermathecal cells are lined with circumferential actin bundles [19] and spermathecal constriction is dependent on the balance between the activity of Rho-kinase and myosin light-chain phosphatase [20]. Biochemical signaling involving inositol 1,4,5-triphosphate (IP3)-mediated calcium release also represents an important component in the cyclic regulation of spermatheca contractility [21]. This is evident from studies conducted in mutants defective in the calcium-signaling pathway [22–24]. Although components involved in spermathecal constriction have been identified, the mechanism regulating the timing of constriction initiation remains elusive.

Here, we identified a RhoGAP protein, spermatheca physiology variant 1 (SPV-1), which utilizes an F-BAR domain to transiently bind the apical membrane, presumably by sensing changes in membrane curvature. In the absence of an oocyte, the spermatheca resembles a deflated balloon with heavily convoluted membrane folds lining the collapsed lumen (www.wormimage.org). During ovulation, stretching of the spermatheca cells by the incoming oocyte [19, 21] serves as an intrinsic mechanism to modulate cell membrane curvature. Spatiotemporal control of SPV-1 localization ensures that RHO-1/RhoA activity rises at the correct time after

*Correspondence: biezbr@nus.edu.sg

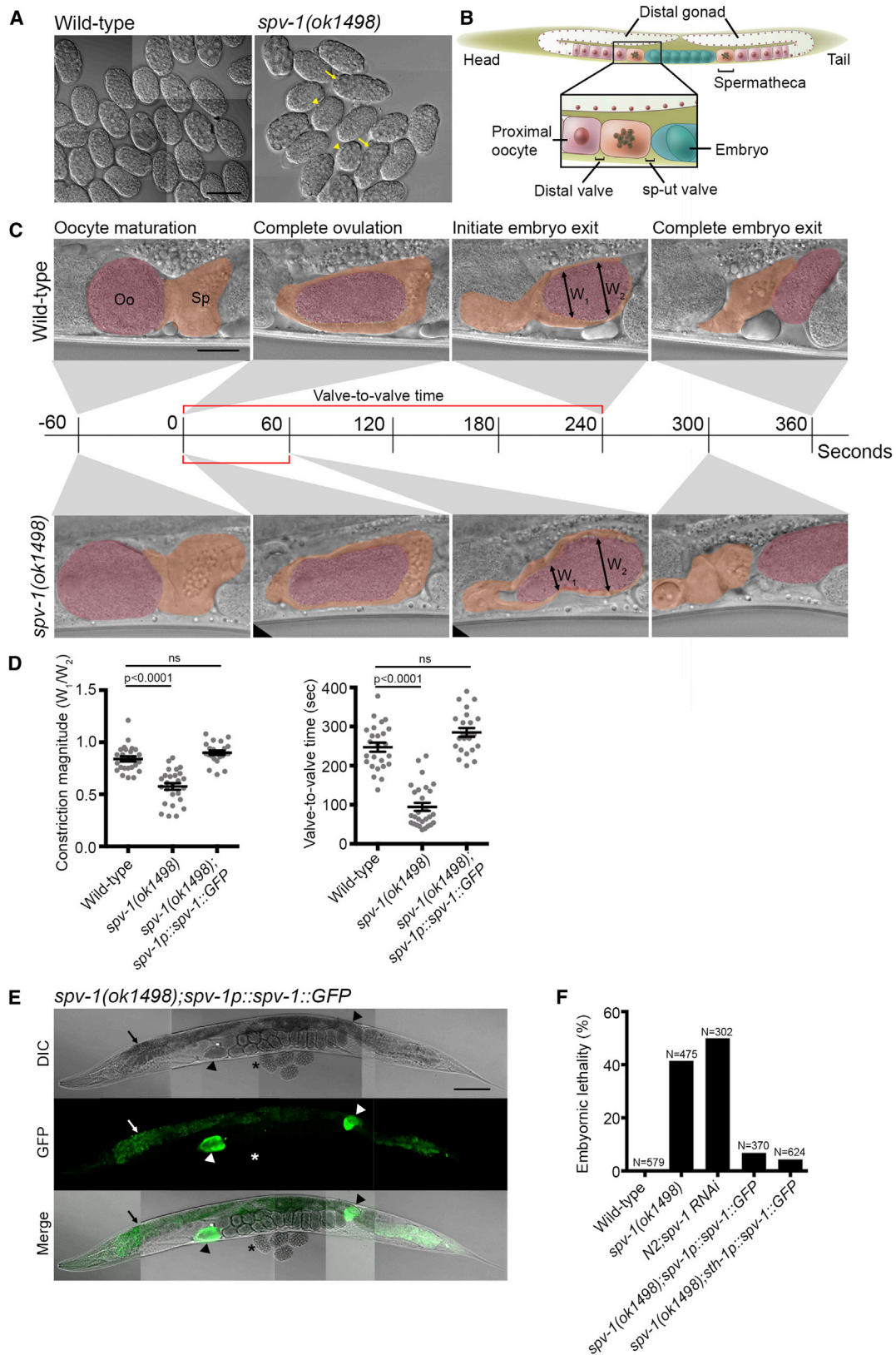


Figure 1. SPV-1 Regulates Spermatheca Contractility

(A) Wild-type and *spv-1(ok1498)* mutant embryos. Arrows and arrowheads indicate elongated and round embryos, respectively. See also Figure S1. Scale bar, 50 μ m.

(B) Schematic of *C. elegans* hermaphrodite reproductive system. Inset shows the region imaged in (C).

(legend continued on next page)

ovulation. Hence, we propose that SPV-1 serves as a mechanotransducer linking changes in membrane curvature to the regulation of RHO-1 activity and downstream actomyosin contraction.

Results

SPV-1 Is a Regulator of Spermatheca Contractility

In an RNAi screen of *C. elegans* RhoGAPs, we found SPV-1 to be essential for embryonic viability and for the generation of embryos with normal shape. We confirmed these phenotypes using a 577 bp frameshift deletion allele of *spv-1*, *ok1498*, which lacks part of the RhoGAP domain. The stereotypical geometry of wild-type *C. elegans* embryos is a prolate ellipsoid of revolution with an axial ratio of 1.69 (mean) \pm 0.014 (SEM) ($n = 50$) (Figure 1A; Figure S1A available online). In contrast, *spv-1(ok1498)* or *spv-1(RNAi)* knockdown resulted in embryos of irregular geometries and sizes with axial ratios ranging from 1.00 to 2.83 ($n \geq 50$), and 41% of *spv-1(ok1498)* and 50% of *spv-1(RNAi)* embryos failed to hatch ($n > 300$) (Figure 1A; Figure S1A). Interestingly, we observed a bias of developmental arrest in embryos with axial ratios below 1.69 (Figure S1A). Previous studies reported that misregulation of spermatheca contractility can give rise to embryos of aberrant geometries [19, 25]. We therefore analyzed the transit of embryos through the spermatheca, using live differential interference contrast (DIC) microscopy, to compare the spermatheca function between wild-type and *spv-1(ok1498)* hermaphrodites. Figure 1B illustrates the *C. elegans* gonad, and the enlarged region indicates the field of imaging. Figure 1C shows representative images from such movies. Ovulation, the passage of the most proximal oocyte from the gonad into the spermatheca, took 1 min in both wild-type and *spv-1(ok1498)* worms (Figure 1C). Complete ovulation is defined by the closure of the distal spermatheca valve and is referred to as time 0. Oocyte entry into the spermatheca is known to be closely followed by fertilization [18]. In the wild-type hermaphrodite, the newly fertilized embryo resided in the spermatheca for 240 s before the spermatheca constricted and propelled the embryo into the uterus through the opening of the spermatheca-uterine (sp-ut) valve (Figure 1C; Movie S1). In contrast, the spermatheca of the *spv-1(ok1498)* mutant began to display a constricted morphology after only 60 s and forced a premature exit of the embryo into the uterus (Figure 1C; Movie S2). Despite the precocious and excessive contraction of the spermatheca in *spv-1* mutant worms, the average time for embryos to completely exit the spermatheca in *spv-1(ok1498)* (115.8 \pm 13.84, $n = 24$) is not significantly different from wild-type (92.35 \pm 12.84, $n = 23$) (Figure S1B). This is because, whereas some embryos transit through the mutant spermatheca more rapidly than wild-type, others become trapped by the overconstricted spermatheca for extended periods of time, as shown in Figure S1C, and occasionally they are severed by the spermatheca.

To quantify the magnitude of spermathecal constriction, we measured the width at its distal (W_1) and proximal quarters (W_2) prior to opening of the sp-ut valve and calculated their ratio. A nonconstricted spermatheca will have a W_1/W_2 ratio close to one, whereas constriction of the distal spermatheca will result in ratios lower than one. Quantification of the constriction magnitude in *spv-1(ok1498)* worms ($n = 28$) showed a 31% increase in constriction ($p < 0.0001$) compared to wild-type spermatheca ($n = 25$) (Figure 1D). We also quantified the valve-to-valve time, defined as the time between complete closure of the distal spermatheca valve and opening of the sp-ut valve. Closure of the distal valve signifies the completion of ovulation, and the opening of the sp-ut valve accompanies the beginning of spermathecal contraction. The mean valve-to-valve time in *spv-1(ok1498)* mutants (94.5 \pm 10.3 s, $n = 28$) was significantly shorter than in wild-type animals (247.2 \pm 11.61 s, $n = 25$) ($p < 0.0001$), confirming that spermatheca constriction not only is stronger in the mutant, but also has an earlier onset (Figure 1D). Precocious constriction of the spermatheca in *spv-1(ok1498)* mutants is also evident by following the change in constriction magnitude over the course of a single-embryo transit event in both wild-type and mutant worms (Figure S1D) ($n = 7$). In the wild-type worms W_1/W_2 gradually increased and plateaued before slightly decreasing prior to sp-ut valve opening. In contrast, the width of the spermatheca in the *spv-1(ok1498)* worms decreased as soon as the oocyte completed ovulation and continued to decrease until embryo exit ($n = 7$) (Figure S1D).

Given the apparent function of SPV-1 in the spermatheca, we sought to determine its expression pattern. To this end, we constructed a translational fusion of SPV-1 with GFP driven by its endogenous promoter. We observed SPV-1::GFP to be expressed exclusively in the spermathecal cells (Figure 1E, arrowheads). Importantly, the full-length translational construct successfully rescued all the mutant phenotypes: spermathecal constriction magnitude and valve-to-valve time were restored to wild-type levels ($n = 23$) (Figure 1D); embryonic lethality was eliminated ($n = 370$) (Figure 1F), and embryo morphology was restored to wild-type dimensions (Figure S1E). It is worth noting that 48% of the embryo transit events did not result in complete embryo exit, probably due to overexpression of SPV-1::GFP. The fact that we did not observe expression of SPV-1::GFP in embryos (Figure 1E, asterisk) suggested that the embryonic lethality associated with loss of *spv-1* function is solely due to the aberrant spermatheca activity and is a consequence of abnormal embryo shapes. To confirm this, we drove *spv-1* expression using the spermatheca-specific promoter of *sth-1* [26] in *spv-1(ok1498)* worms. As expected, spermathecal expression alone was sufficient to rescue embryonic lethality along with the embryo shape defect (Figure 1F; Figure S1E). Furthermore, we crossed *spv-1(ok1498)* hermaphrodites with either wild-type or *spv-1(ok1498)* males and scored for embryonic lethality. A slight reduction in embryonic lethality was

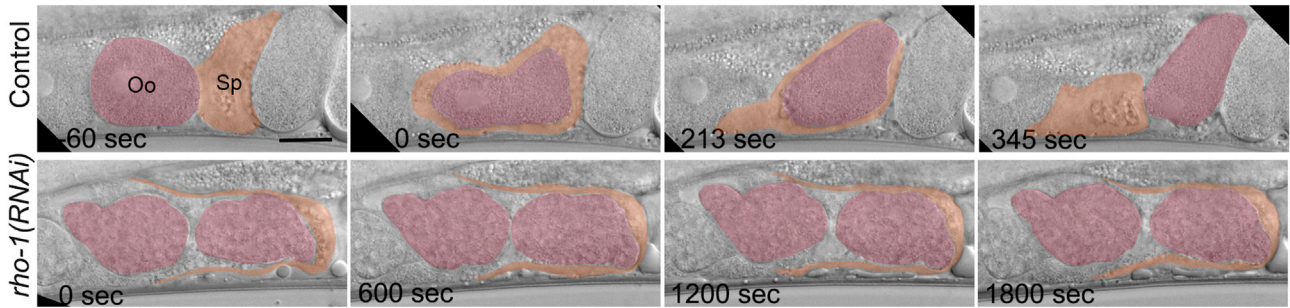
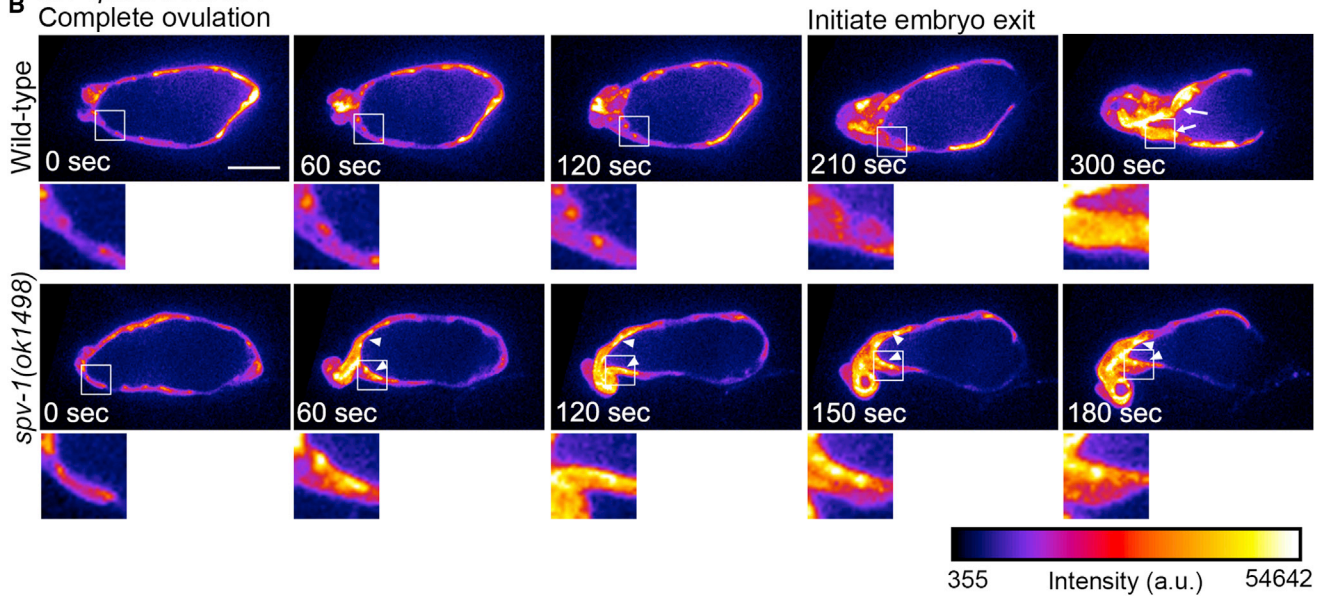
(C) Representative ovulation and embryo transit events in wild-type and *spv-1(ok1498)* animals. Complete closure of the distal valve (complete ovulation) is referred to as time 0. Valve-to-valve time is defined by the interval between distal valve closure and opening of the spermatheca-uterine valve. Oo, oocyte; Sp, spermatheca. Scale bar, 20 μ m.

(D) Quantification of constriction magnitude and valve-to-valve time in wild-type, *spv-1(ok1498)*, and SPV-1::GFP transgenic line. Constriction magnitude is the measurement of the ratio between distal (W_1) and proximal (W_2) spermatheca widths. Data are represented as individual embryo transit events (gray dots) with mean \pm SEM. $n \geq 23$ for each worm strain analyzed. Statistical comparisons were performed using one-way ANOVA-Tukey's multiple comparisons test.

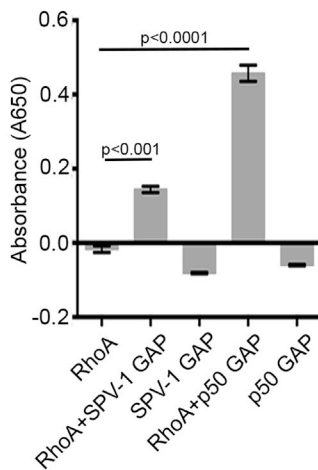
(E) SPV-1 expression pattern. SPV-1::GFP under the regulation of its endogenous promoter is expressed in the spermatheca (arrowheads). Arrows indicate autofluorescence of the gut granules. Asterisk denotes the embryos. Scale bar, 100 μ m.

(F) Quantification of embryonic lethality in *spv-1* loss-of-function and after restoration of SPV-1 function. N indicates the number of embryos analyzed.

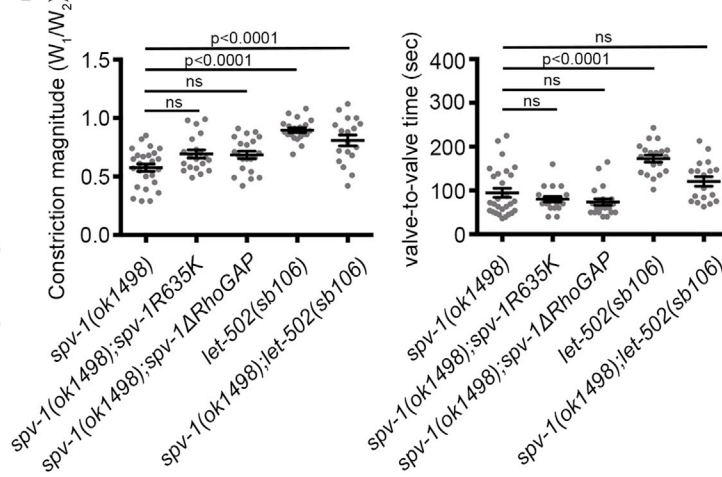
A Wild-type

B *sth-1p::AHPH::GFP*
Complete ovulation

C



D



E

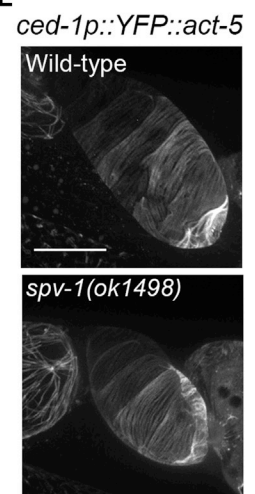


Figure 2. SPV-1 Functions Upstream of the RhoA-ROCK Pathway

(A) Effect of RHO-1 knockdown on embryo transit through the spermatheca. Representative images taken from movies of control (L4440) and *rho-1(RNAi)* treated animals. The spermatheca (highlighted in orange) in the *rho-1(RNAi)* animal did not contract during the 30 min imaging period, and two embryos (highlighted in pink) can be seen trapped within it. Oo, oocyte; Sp, spermatheca. Scale bar, 20 μ m.

(B) Live imaging of active RHO-1 biosensor (AHPH::GFP) in wild-type and *spv-1(ok1498)* spermathecae. Arrows and arrowheads indicate an accumulation of AHPH::GFP. Scale bar, 20 μ m.

(C) In vitro RhoGAP activity assay measuring GAP activity toward recombinant mammalian RhoA shows GAP activity of the RhoGAP domain of SPV-1.

(legend continued on next page)

observed in cross-progeny regardless of the genotype of the males, indicating that the partial paternal rescue (possibly due to an unknown relaxing effect of male sperm on the spermatheca) was not due to the presence of a zygotic copy of wild-type *spv-1* (Figure S1F). Thus, SPV-1 is a newly discovered regulator of spermatheca contractility, and in this capacity it has a profound impact on embryonic viability.

SPV-1 Regulates Contractility through the RHO-1/RhoA-LET-502/ROCK Pathway

Because SPV-1 has a putative RhoGAP domain, we postulated that SPV-1 functions to regulate RHO-1 activity in the spermatheca. However, the contribution of RHO-1 to spermatheca contractility has not yet been reported. To test the consequence of reducing RHO-1 levels on spermatheca contractility, we performed partial *rho-1* knockdown using feeding RNAi. Knockdown of *rho-1* for 36 hr resulted in complete loss of spermathecal contractility and embryos being trapped in the spermatheca (n = 14) (Figure 2A). Importantly, a milder 24 hr *rho-1* RNAi treatment in the mutant background rescued the *spv-1(ok1498)* hypercontractile phenotype and restored normal embryo transit (n = 4) (Figure S2A), suggesting that the early and hypercontractile spermathecal phenotypes we observed in *spv-1* loss of function were due to excessive RHO-1 activity. To directly test this possibility, we utilized a recently established RHO-1 activity reporter comprising of the Rho-binding domain of *C. elegans* anillin ANI-1 (AHPH) [27] fused to GFP to monitor RHO-1 activity in the spermatheca during embryo transit. In wild-type worms, we observed a gradual increase in the intensity of the active RHO-1 sensor at the distal end of the spermatheca during the time between distal valve closure to the opening of sp-ut valve, and the intensity peaked during embryo exit (Figure 2B, arrows). In contrast, the spermatheca of *spv-1(ok1498)* worms displayed an immediate accumulation of the active RHO-1 sensor upon distal valve closure (Figure 2B, arrowheads). We confirmed the efficacy of the RHO-1 sensor by knocking down *rho-1* in the *spv-1(ok1498)* worms carrying the RHO-1-biosensor. As shown in Figure S2B, under these conditions a premature accumulation of the biosensor at the distal end of the spermatheca was not observed. These results indicate that SPV-1 normally functions to suppress the level of active RHO-1 in the spermatheca during the initial stages of embryo transit.

To demonstrate that the RhoGAP domain of SPV-1 directly regulates Rho activity, we performed an in vitro RhoGAP activity assay using purified recombinant proteins. As expected, the RhoGAP domain of SPV-1 was able to enhance the hydrolysis of GTP to GDP by mammalian RhoA (Figure 2C). To establish that the RhoGAP domain is essential for SPV-1 function in vivo, we introduced into *spv-1(ok1498)* worms full-length SPV-1 engineered with a nonfunctional RhoGAP domain, SPV-1(R635K)::GFP. Transgenic mutants carrying the dead-GAP construct were indistinguishable from *spv-1(ok1498)* mutants alone in terms of spermatheca constriction magnitude and valve-to-valve time (Figure 2D). Similar results were obtained with a complete truncation of the RhoGAP domain (Figure 2D). These results confirm the importance of the RhoGAP catalytic domain of SPV-1 in maintaining low

levels of RHO-1 activity in the spermatheca in the first few minutes of embryo transit.

Based on work in other systems, it is well established that RhoA can regulate actomyosin contractility via two independent pathways: (1) activation of formins, which leads to actin filament polymerization; (2) activation of Rho-kinase, which leads to myosin activation through phosphorylation of MLC and MLCP [6–9]. To determine whether elevated RHO-1 activity in the spermatheca results in changes to the circumferential actin bundles, we visualized actin filaments using a YFP::ACT-5 reporter. As shown in Figure 2E, there was no discernable difference between the actin structures of mutant and wild-type spermathecae at the resolution of the light microscope. Next, we tested the involvement of *let-502*/Rho-Kinase in mediating the effects of RHO-1 in the spermatheca. To this end, we performed a genetic cross between *spv-1(ok1498)* and *let-502(sb106)*, a Rho-kinase hypomorph [28]. Importantly, the overconstriction phenotype was alleviated in the double mutant, suggesting that SPV-1 functions upstream of Rho-kinase (Figure 2D). Taken together, our results suggest that the RhoGAP domain of SPV-1 plays an essential role in regulating spermatheca contractility via the RhoA-ROCK pathway.

SPV-1 Localization at the Apical Membrane of Spermatheca Cells Is Transient

The subcellular localization pattern of SPV-1 during embryo transit was determined by live imaging of SPV-1::GFP using confocal microscopy (Figure 3A). During the initial phase of embryo transit (0 s) we observed SPV-1 to be enriched at the apical membrane. Importantly, the membrane signal progressively diminished and disappeared (180 s) prior to the opening of the sp-ut valve (360 s) (Figure 3A). To understand the temporal relationship between the loss of apical SPV-1, the rise in RHO-1, and the initiation of spermatheca constriction, we quantified the enrichment of SPV-1::GFP at the membrane, from the completion of ovulation until the initiation of embryo exit, and plotted these data alongside the quantification of RHO-1 levels using the same temporal framework (Figure 3B). This analysis clearly showed that levels of membrane-bound SPV-1 began to diminish immediately after ovulation, and no membrane enrichment was detected halfway through the embryo retention period (membrane/cytoplasm ratio of 1). Concomitant with the loss of SPV-1 from the membrane, RHO-1 levels gradually increased, and at the midpoint of the embryo retention period, RHO-1 levels began to climb more rapidly, reaching a maximum when embryo exit was complete (Figure 3B).

A Novel F-BAR Domain in SPV-1 Mediates Membrane Binding

To elucidate the molecular mechanism responsible for the transient binding of SPV-1 to the membrane, we performed a bioinformatics analysis on the amino acid sequence of SPV-1. A conserved domain search [29] revealed an N-terminal Fes/Cip4 homology (FCH) and phorbolesters/diacylglycerol binding (C1) domains in addition to the RhoGAP domain (Figure 4A, top panel). Coiled-coil motif analysis [30] predicted the presence of a coiled-coil (CC) region closely following the FCH domain (Figure 4A, top panel). Taken together, an FCH domain

(D) Quantification of the constriction magnitude and valve-to-valve time for transgenic worms depleted of RhoGAP activity and Rho-kinase hypomorphs, *let-502(sb106)*. Quantification for *spv-1(ok1498)* is duplicated from Figure 1F. Data are represented as individual embryo transit events (gray dots) with mean \pm SEM. n \geq 18 for each worm strain analyzed. Statistical comparisons were performed using one-way ANOVA-Tukey's multiple comparisons test. (E) Circumferential actin bundles in wild-type and *spv-1(ok1498)* mutant spermatheca visualized with YFP::ACT-5. Scale bar, 20 μ m

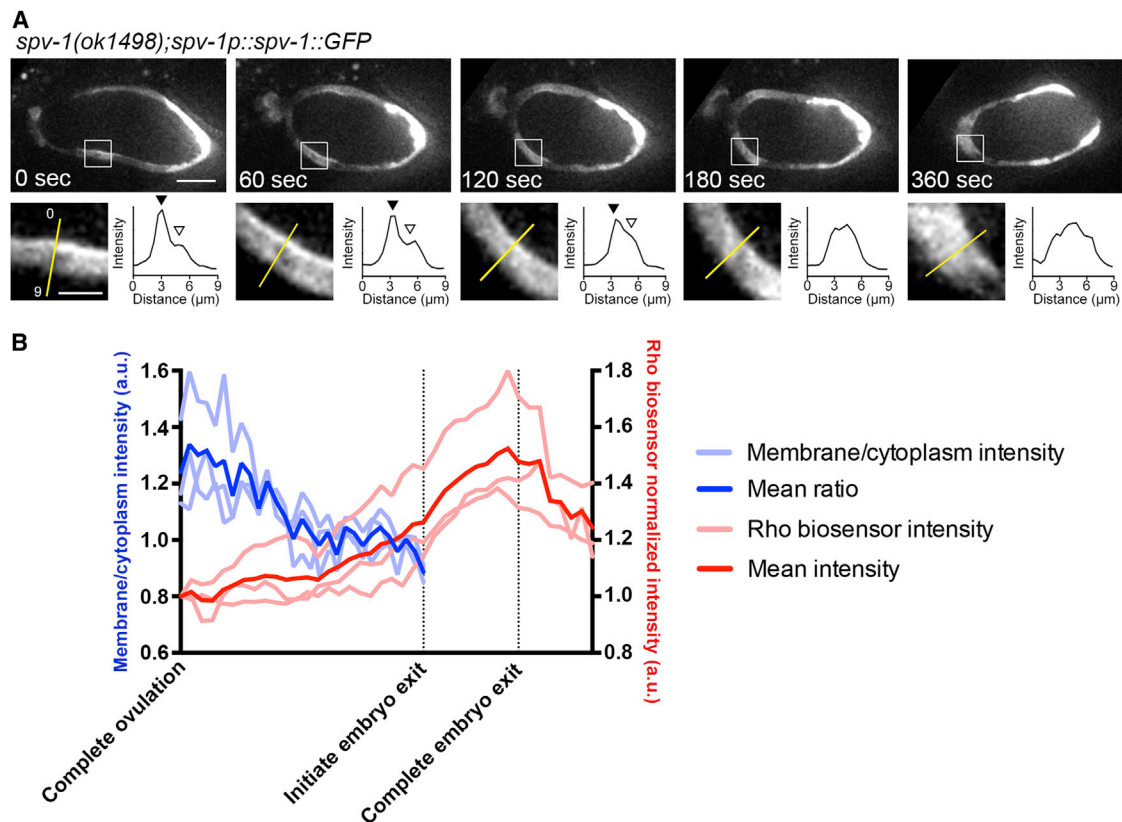


Figure 3. SPV-1 Transiently Localizes to the Plasma Membrane

(A) Representative images of SPV-1::GFP subcellular localization during embryo transit. Graphs show the intensity profile of lines drawn perpendicular to the spermatheca cells. Black and white arrowheads highlight the differences in intensity between the cell edge and cytoplasm. Scale bars: whole spermatheca, 20 μm ; inset, 5 μm .

(B) Quantification of SPV-1::GFP membrane accumulation and AHPH::GFP total intensity during embryo transit. The valve-to-valve time (time interval between completion of ovulation and initiation of embryo exit) on the x axis is normalized to a scale of 0–1 to enable the line plots to be superimposed on the same graph. Light-colored lines represent individual embryo transit events; bold lines are mean values quantified from the light-colored lines. See [Supplemental Experimental Procedures](#) for details on quantifications.

followed by a coiled-coil region indicates the presence of a putative F-BAR domain [31–33]. [Figure 4A](#) (bottom panel) shows the predicted structure of SPV-1 modeled using the default intensive setting of Phyre2 [34]. Using Domain Enhanced Lookup Time Accelerated Basic Local Alignment Search Tool (DELTA-BLAST) [35], we identified orthologs of SPV-1, which included the putative F-BAR domain, in all metazoan genomes searched from sponges to mammals ([Figure 4B](#)). Interestingly, we also identified an ortholog in the premetazoan *Monosiga brevicollis* (XP_001748029.1), but none in Fungi or Amoeba. There appears to be a single SPV-1 ortholog in each metazoan species up to chordates, whereas vertebrates have three orthologs. The three human orthologs are the GEM interacting protein (GMIP), Rho GTPase-activating protein 29 (ARHGAP29, also known as PARG1), and minor histocompatibility protein HA-1 (HMHA1). GMIP and ARHGAP29 have not been characterized to have an F-BAR domain, whereas HMHA1 was recently reported to harbor a BAR domain [36]. Phylogenetic analysis of previously described F-BAR domains and SPV-1 orthologs indicates that the F-BAR domain of SPV-1 and its orthologs form a distinct class of F-BAR domains ([Figure 4C](#)).

We used the 2.4 \AA crystal structure of the N-terminal domain of human GMIP (PDB ID: 3QWE) as a template to predict the

structure of the F-BAR domain of SPV-1 using I-TASSER [37]. [Figure 4D](#) shows two views of the predicted structure of a putative dimer formed by two SPV-1 F-BAR domains. The side view (top panel) shows that the F-BAR dimer is predicted to form a shallow concave curvature, as expected for F-BAR domains. The bottom panel, which shows the membrane-interacting surface of the F-BAR dimer, highlights the high number of positive amino acid residues along this surface, which are expected to interact with the negatively charged membrane.

To experimentally test the role of the F-BAR domain in localizing SPV-1 transiently to the plasma membrane, we created an SPV-1 construct lacking its F-BAR domain (*spv-1p::spv-1 Δ F-BAR::GFP*) and examined its localization pattern in the mutant background. As expected, membrane localization of SPV-1 was abolished in the absence of the F-BAR domain ([Figure S3A](#)). However, the expression of the Δ F-BAR construct was dramatically reduced compared to the full-length protein. To circumvent this problem, we drove SPV-1 Δ F-BAR::GFP under the *sth-1* promoter, which gave higher expression. Even with higher expression, SPV-1 Δ F-BAR::GFP remained strictly cytoplasmic ([Figure 4E](#)). Interestingly, loss of membrane localization did not affect the RhoGAP activity of the truncated protein but rather prolonged the valve-to-valve

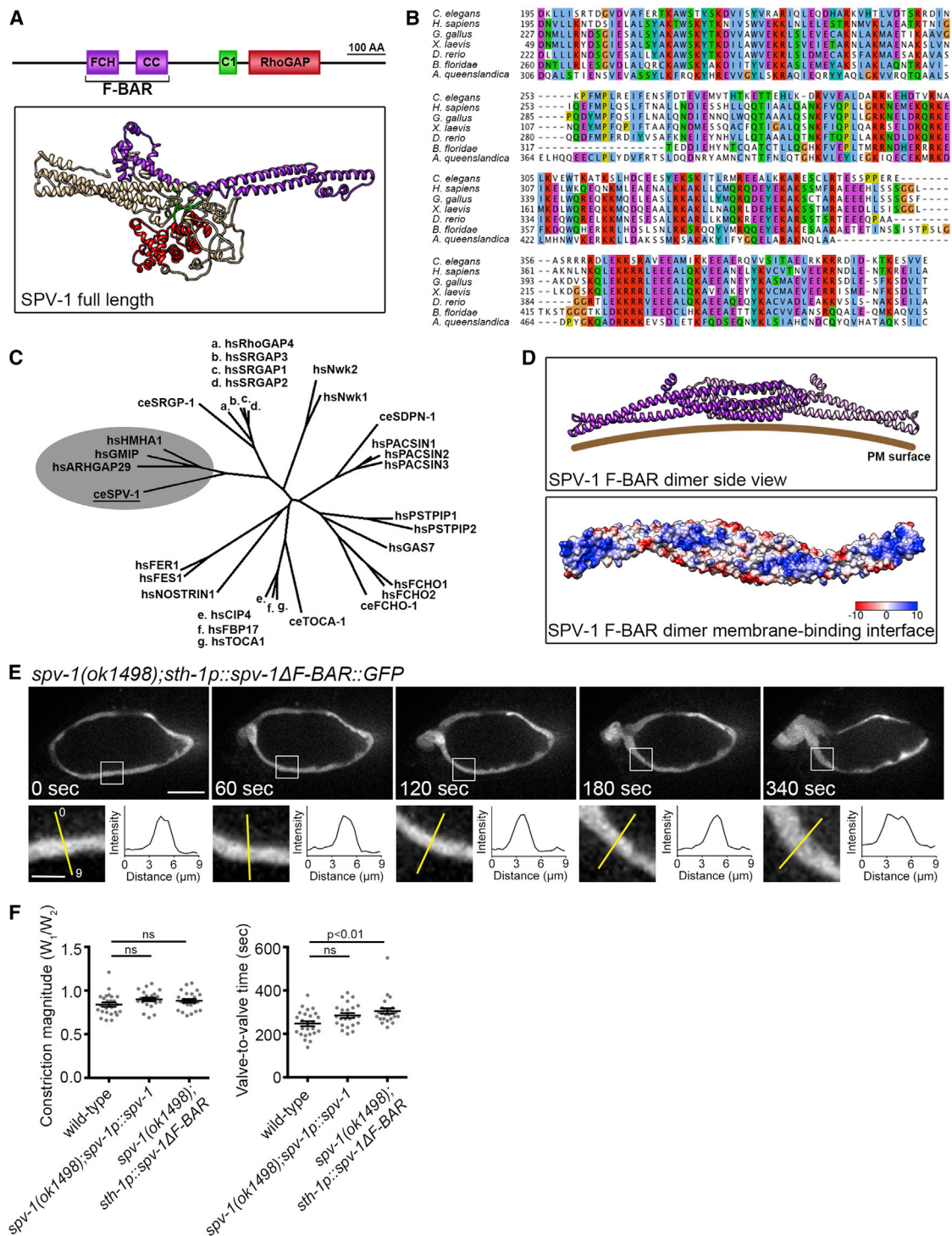


Figure 4. F-BAR Domain of SPV-1 Mediates Membrane Binding

(A) Top panel, protein domains of SPV-1. Bottom panel, predicted protein structure of SPV-1. Purple, F-BAR domain; green, C1 domain; red, RhoGAP domain.

(B) Multiple sequence alignment of the F-BAR domain of a selection of SPV-1 orthologs from sponges to mammals. See Table S1 for the NCBI reference sequences. Blue, A, I, L, M, F, W, V, and C; red, R and K; green, N, Q, S, and T; pink, C; magenta, E and D; orange, G; cyan, H and Y; yellow, P. Refer to <http://www.jalview.org/help/html/colourSchemes/clustal.html> for the full color scheme.

(C) Unrooted phylogenetic tree depicting human F-BAR domains and selected *C. elegans* orthologs. The F-BAR domain of SPV-1 and its human orthologs (HMHA1, GMIP, and ARHGAP29) form a distinct group (gray cloud). *ce*, *C. elegans*; *hs*, *H. sapiens*. See Table S2 for a list of NCBI reference sequences.

(D) Predicted structure of the F-BAR dimer. Top panel shows the side view of a ribbon representation. Bottom panel shows the membrane-interacting surface with positive amino acid residues highlighted in blue and negative residues in red.

(E) Representative images of SPV-1ΔF-BAR::GFP driven by the *sth-1* promoter showing its subcellular localization during embryo transit.

(legend continued on next page)

time as compared to wild-type worms (Figure 4F). We hypothesize that the F-BAR domain, when not bound to the membrane, inhibits the RhoGAP activity either through direct interaction, or by steric hindrance. An inhibitory role for an F-BAR domain on RhoGAP and other domains, such as SH3, has been previously reported for other F-BAR proteins [38, 39]. Recently, de Kreuk et al. reported that the RhoGAP activity of HMHA1, which we identified as one of the human orthologs of SPV-1, is autoinhibited by its BAR domain because only mutants lacking the BAR domain showed GAP activity toward RhoGTPases [36]. This supports the idea that deletion of the F-BAR domain may have created an SPV-1 with constitutive RhoGAP activity, which could explain its ability to rescue the mutant. However, our attempts to detect an interaction between the N (F-BAR-containing) and C (RhoGAP-containing) terminus of SPV-1 in a pull-down assay, using bacterially synthesized protein fragments, were unsuccessful.

Taken together, bioinformatics, structural prediction, and localization experiments indicate that SPV-1 harbors a novel highly conserved F-BAR domain that mediates its binding to the plasma membrane.

Transient Membrane Localization of SPV-1 Is Required for Embryo Transit through the Spermatheca

The evidence thus far suggested that spermatheca stretching by an incoming oocyte, sensed by the F-BAR domain, leads to SPV-1 detachment from the plasma membrane and subsequent increase in RHO-1 and spermatheca contraction. As a test of this model, we investigated the consequence of constitutively localizing SPV-1 to the membrane. For this purpose, we substituted the F-BAR domain with a pleckstrin homology (PH) domain from rat phospholipase C gamma 1 (PLC1 σ 1) and introduced the chimeric SPV-1::GFP construct into the mutant worm. The transgenic worms displayed permanent SPV-1::GFP localization on the apical membrane of spermatheca cells (Figure 5A). Notably, instead of a single embryo per spermatheca transiting within approximately 6 min in wild-type worms, each spermatheca we observed in the strain expressing constitutive membrane-bound SPV-1 was occupied by multiple embryos and none of the embryos exited the spermatheca during the 30 min imaging period ($n = 10$) (Figures 5A and 5B; Movie S3). These results indicate that prolonged attachment of SPV-1 to the membrane hinders the initiation of spermatheca contractility, most likely due to reduced RHO-1 activity at the plasma membrane. Thus, detachment of SPV-1 from the membrane, facilitated by the F-BAR domain, functions as a cue to initiate spermathecal contractility and embryo exit.

Discussion

Taken together, our findings support a model in which SPV-1 regulates cyclical contraction of the spermatheca through transient localization to the apical membrane mediated by its F-BAR domain (Figure 5C). We presume SPV-1 localization to be membrane curvature dependent. When localized to the membrane, SPV-1 inhibits contractility by inactivating RHO-1

through its RhoGAP domain. Oocyte entry stretches the spermatheca cells, straightening out membrane curvature, and thus leads to detachment of SPV-1, which, in turn, permits the level of active RHO-1 to rise beyond a threshold needed to induce contraction. An alternative explanation for SPV-1's transient localization, which we cannot rule out, is that soluble signals from the oocyte induce a change in the spermatheca apical membrane that leads to SPV-1 detachment.

Egg Shape Has Consequences for Embryonic Development

We identified *spv-1* as a gene that, when knocked down, resulted in embryos with aberrant shape and 50% embryonic lethality. Interestingly, we did not detect SPV-1::GFP expression in embryos. Crossing *spv-1(ok1498)* hermaphrodites with wild-type males did not rescue the embryonic phenotypes any more than crossing with *spv-1(ok1498)* males, suggesting SPV-1 function is required in the mother and not in the embryo. Consistent with that, driving SPV-1::GFP expression in the spermatheca of *spv-1(ok1498)* using the *sth-1* promoter not only rescued spermatheca contractility and embryo shape defects, but also completely restored the viability of the embryos. Thus, we concluded that lethality in *spv-1(RNAi)* and *spv-1(ok1498)* embryos is entirely due to their abnormal shape. Premature arrest in embryonic development could be caused by loss of cytoplasmic material as a result of embryos being severed by overconstriction of the spermatheca, resulting in small embryos. Another possible explanation for embryo arrest could be the deviation from the normal geometric shape. As evident in Figure S1A, abnormally long embryos developed normally, whereas the rounder-than-normal embryos were likely to arrest. The mechanistic relationship between embryo shape and development in *spv-1* mutants is a topic for future investigation.

The F-BAR Domain of SPV-1, along with Its Metazoan Orthologs, Forms a Novel Class of F-BAR Domains

Using DELTA-BLAST, we identified orthologs of SPV-1 in all metazoan genomes we searched, as well as in the premetazoan choanoflagellate *M. brevicollis*. The F-BAR domain we identified in SPV-1 is well conserved in all its orthologs, including the three human orthologs: ARHGAP29, GMIP, and HMHA1. A phylogenetic analysis of SPV-1's F-BAR domain along with all known human F-BAR domains showed that the F-BAR domain of SPV-1 orthologs form a distinct subfamily, which may explain why they have not been recognized as such to date, despite the fact that the crystal structure of GMIP's N terminus has been solved and displays a distinct F-BAR fold. It will be interesting to test if the F-BAR domain of SPV-1 orthologs also sense and selectively bind to curved membranes in vivo, which might provide a mechanism to regulate RhoGAP localization in mammalian cells.

Interplay between Calcium Signaling and RhoA Pathway in Contractile Tubes

The myoepithelial spermathecal pouch in *C. elegans* is analogous in terms of structure and function to contractile smooth

See also Figure S3. Graphs show the intensity profile of lines drawn perpendicular to the spermatheca cells. Scale bar, whole spermatheca, 20 μ m; inset, 5 μ m.

(F) Quantification of constriction magnitude and valve-to-valve time in wild-type and *spv-1(ok1498)* worms expressing either full-length SPV-1::GFP or SPV-1 Δ F-BAR::GFP.

Data are represented as individual embryo transit events (gray dots) with mean \pm SEM. $n \geq 23$ for each worm strain analyzed. Wild-type values are duplicated from Figure 1D. Statistical comparisons were performed using one-way ANOVA-Tukey's multiple comparisons test.

A *spv-1(ok1498); spv-1p::spv-1ΔF-BAR(PH)::GFP*

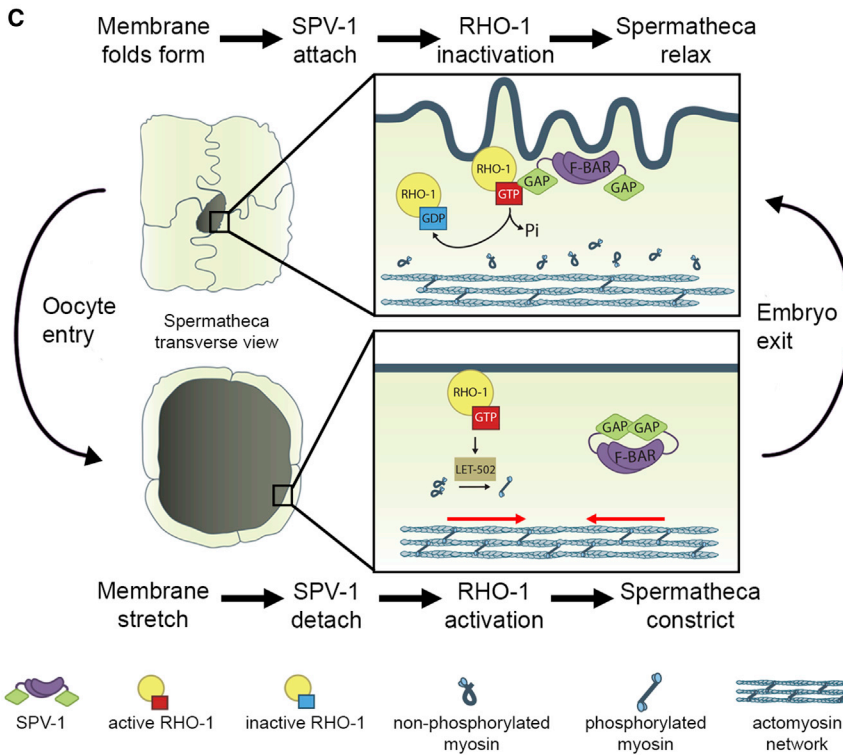
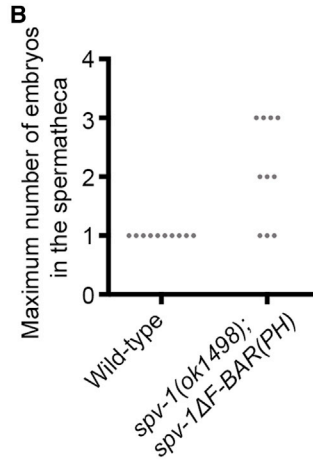
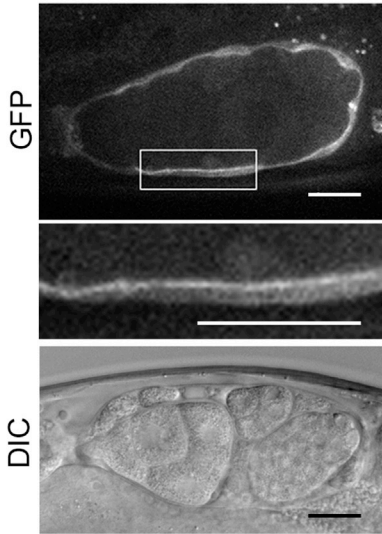


Figure 5. Transient Localization of SPV-1 Is Essential for Embryo Transit

(A) Representative images of transgenic worm spermatheca with chimeric SPV-1::GFP. The F-BAR domain of SPV-1 was replaced with a PH domain. The GFP panels indicate membrane localization, whereas the DIC panel displays multiple embryos in the spermatheca. Scale bar, 20 μ m.

(B) Quantification of the maximum number of embryos in the spermatheca during a 30 min imaging period. Each dot represents an independent experiment. $n = 10$ for each strain.

(C) Model illustrating the mechanism of spermatheca contractility regulation by transient localization of SPV-1 at the membrane.

rise in calcium levels in the spermatheca, triggered by oocyte entry and stretching of the spermatheca cells, initiates the constriction of the spermatheca and embryo exit [21]. The oocyte entry-dependent calcium release is regulated by PLC-1 and its downstream partners, raising the possibility that PLC-1 could be under the regulation of RHO-1, as suggested by studies in mammalian cells [42]. It remains to be seen if SPV-1, identified as a negative regulator of RHO-1, could modulate calcium release in addition to regulation of spermatheca contractility via the RHO-1/LET-502 pathway.

Plasma Membrane as a Site of Mechanical Regulation of RhoA

Tension-sensitive ion channels in prokaryotes provided the earliest evidence for the plasma membrane as a site of mechanotransduction. In bacterial cells, the mechanosensitive channel of large conductance (MscL) opens under high osmotic pressure to allow the exit of large solutes from cells to prevent cell lysis [43]. More recently, the idea of plasma membrane tension as a mechanical cue to coordinate cell-shape change in eukaryote cells has garnered evidence [44–46]. Quantitative modeling of keratocyte migration suggested that forces imposed on the actin network by the membrane play an essential role in regulating actin assembly at the front and disassembly at the rear of the cell,

muscle tubes in mammals, such as the respiratory tract, blood vessels, and salivary ducts. Abnormal smooth muscle contractions in these tissues result in severe pathological conditions such as asthma and hypertension. Both RhoA and calcium signaling have been implicated in regulation of the constriction of airway smooth muscle cells and blood vessels [40]. Although these two pathways have long been established, they are usually identified as two independent pathways, converging at the level of myosin light-chain phosphorylation [40, 41]. Recently, Kovacevic et al. reported that a

highlighting the importance of membrane tension in determining the shape of motile cells [47]. Using single-cell spreading assays, Gauthier and colleagues have documented a temporary spike in membrane tension after the initial cell-spreading phase, which is followed by cycles of actomyosin contractility and lamellipodia protrusion at the cell edge, together with deposition of focal adhesions [48]. Coupling of membrane curvature-sensitive domains to GAPs and GEFs may provide a mechanism for regulating small GTPases through a mechanical signal. In the case of ADP ribosylation

factor (ARF)GAP1, presence of an ARFGAP1 lipid-packing sensor (ALPS) domain, which binds favorably to positively curved membranes, together with a GAP domain have been reported to hydrolyze the GTP of ARF in a curvature-dependent manner during coat protein I (COPI) disassembly on Golgi membranes [49]. However, molecular mechanisms that link mechanical properties of the membrane to biochemical pathways regulating actomyosin contractility have remained elusive.

Based on our findings, we propose that SPV-1 functions as a transducer of mechanical cues from the membrane to regulate RHO-1-mediated contractility. It is very attractive to speculate that coupling of a membrane curvature-sensitive domain to RhoGAPs could function as a universal mechanism to feedback between membrane curvature and initiation of actomyosin contractility to drive cell-shape change during cell migration or other morphogenic events.

Experimental Procedures

C. elegans Strains and Worm Culture

C. elegans strains were grown on nematode growth medium (NGM) agar seeded with OP50 *Escherichia coli* at 20°C, unless otherwise specified. Refer to Table S3 for a full list of strains used in this study. Transgenic strains carrying *msnEx* arrays were generated by injecting DNA into the gonads of adult hermaphrodites. The injection mix contained 5–10 ng/μl of target DNA construct, 100 ng/μl of pBluescript plasmid, and 20 ng/μl of *rol-6(su1006)* plasmid as a coinjection marker. At least two lines were generated and imaged for each strain, except for the RhoGAP dead strain.

C. elegans Cross and Progeny Test

spv-1(ok1498) hermaphrodites were crossed with either *spv-1(ok1498)* or wild-type males for 24 hr. Hermaphrodites were then singled out to lay embryos. Embryos and the resulting hatched progenies were tabulated. F1 progeny with a high incidence of males were considered cross-progeny, and plates with no males were considered as non-cross-progeny and used as controls.

RNAi

RNAi knockdown of gene expression was performed as previously described [50]. Briefly, knockdown of *spv-1* was done by feeding L1 larva with a Vidal library RNAi clone (OpenBioSystems) targeting *spv-1* at 25°C for 48 hr. Worms were fed *rho-1* Ahringer library RNAi clones (Source BioScience) at 20°C for 24 hr and 36 hr in the *spv-1(ok1498)* and wild-type background respectively. Bacterial clones carrying an empty L4440 vector and *par-5* gene were used as negative and positive controls.

Molecular Biology

Refer to Supplemental Experimental Procedures for details of the various constructs engineered.

RhoGAP Assay

The C terminus of SPV-1 containing the GAP domain was purified from bacterial culture using a His tag. The activity of the GAP domain of SPV-1 on RhoA was evaluated using the RhoGAP assay (Cytoskeleton) according to manufacturer's protocol. p50RhoGAP catalytic domain was used as a positive control. Release of inorganic phosphate (P_i) was measured at A₆₅₀ with a spectrophotometer (Tecan).

Bioinformatics

Protein domains of SPV-1 were identified by conducting a conserved domain search [51]. The presence of coiled-coil region was determined by Paircoil2 [30], Phyre2 [34] and I-TASSER [37] were used to predict the structure of full-length and F-BAR domain of SPV-1, respectively. SPV-1 orthologs were identified using DELTA-BLAST [35]. Multiple sequence alignments were performed with T-coffee [52] and visualized using Jalview [53]. Phylogenetic distances were calculated with PHYLIP-NEIGHBOR (MPI Bioinformatics Toolkit) [54] and unrooted phylogenetic tree was drawn with Dendroscope [55].

Image Acquisition and Analysis

Young adult hermaphrodites with one-row embryos were immobilized for imaging by mounting them on 10% agarose pads on glass slides. Embryo mounts were prepared by excision of embryos from gravid hermaphrodites and mounted onto 3% agarose pads. M9 buffer was used to prevent sample desiccation. Normaski images and movies shown in Figures 1A, 1C, 1E, 2A, and 5A (DIC panel), Figures S1C and S1E, Figure S2A, and Movies S1 and S2 were captured using a wide-field microscope. All other imaging was performed with a spinning-disk confocal microscope. Refer to Supplemental Experimental Procedures for a detailed description of the microscope setup. Quantifications were performed using ImageJ (NIH) by manual selection of the regions of interest. Constriction magnitude was a measurement of distal spermatheca width divided by proximal width. Valve-to-valve time represented the elapsed time between distal valve closure and opening of the sp-ut valve. Intensity changes of the Rho-biosensor was measured by quantifying the mean intensity of the middle focal plane of a spermatheca across time relative to the intensity at the initial time point. Intensity at the membrane and cytoplasm were quantified by manually tracing a line along the cell edge or the cytoplasm. Mean intensity of the lines drawn at the membrane divided by the values obtained for the cytoplasm provided the membrane-to-cytoplasm ratio. Quantitative data sets were subjected to statistical analysis (ordinary one-way ANOVA-Tukey's multiple comparisons test for all figures, except S1B for which a two-tailed unpaired t test was used) and graphs were drawn using the Prism 6 software (GraphPad).

Supplemental Information

Supplemental Information includes Supplemental Experimental Procedures, three figures, three tables, and three movies and can be found with this article online at <http://dx.doi.org/10.1016/j.cub.2014.11.033>.

Acknowledgments

This work was supported by the National Research Foundation Singapore under its NRF fellowship (NRF-RF2009-RF001-074) awarded to R.Z.-B. Some strains were provided by the CGC, which is funded by NIH Office of Research Infrastructure Programs (P40 OD010440). We thank Michael Glotzer (University of Chicago) for the RHO-1 biosensor plasmid. We thank Wong Chun Xi from Science Communications (Mechanobiology Institute, Singapore) for the illustrations in Figures 1B and 5C. We appreciate the help from Thang Dinh Doan (Mechanobiology Institute, Singapore) in the generation of some transgenic strains and help from Anjali Gupta (Mechanobiology Institute, Singapore) and Paul Murray (Columbia University) in generating structure predictions.

Received: July 22, 2014

Revised: October 27, 2014

Accepted: November 13, 2014

Published: December 18, 2014

References

1. Gunst, S.J., Tang, D.D., and Opazo Saez, A. (2003). Cytoskeletal remodeling of the airway smooth muscle cell: a mechanism for adaptation to mechanical forces in the lung. *Respir. Physiol. Neurobiol.* 137, 151–168.
2. Smith, P.G., Roy, C., Zhang, Y.N., and Chaudhuri, S. (2003). Mechanical stress increases RhoA activation in airway smooth muscle cells. *Am. J. Respir. Cell Mol. Biol.* 28, 436–442.
3. Smiesko, V., and Johnson, P. (1993). The arterial lumen is controlled by flow-related shear stress physiology. *News Physiol. Sci.* 8, 34–38.
4. Davies, P.F. (1995). Flow-mediated endothelial mechanotransduction. *Physiol. Rev.* 75, 519–560.
5. Lessey, E.C., Guilluy, C., and Burrridge, K. (2012). From mechanical force to RhoA activation. *Biochemistry* 51, 7420–7432.
6. Watanabe, N., Kato, T., Fujita, A., Ishizaki, T., and Narumiya, S. (1999). Cooperation between mDia1 and ROCK in Rho-induced actin reorganization. *Nat. Cell Biol.* 1, 136–143.
7. Chrzanowska-Wodnicka, M., and Burrridge, K. (1996). Rho-stimulated contractility drives the formation of stress fibers and focal adhesions. *J. Cell Biol.* 133, 1403–1415.
8. Amano, M., Ito, M., Kimura, K., Fukata, Y., Chihara, K., Nakano, T., Matsuura, Y., and Kaibuchi, K. (1996). Phosphorylation and activation of myosin by Rho-associated kinase (Rho-kinase). *J. Biol. Chem.* 271, 20246–20249.

9. Kimura, K., Ito, M., Amano, M., Chihara, K., Fukata, Y., Nakafuku, M., Yamamori, B., Feng, J., Nakano, T., Okawa, K., et al. (1996). Regulation of myosin phosphatase by Rho and Rho-associated kinase (Rho-kinase). *Science* 273, 245–248.
10. Rossman, K.L., Der, C.J., and Sondek, J. (2005). GEF means go: turning on RHO GTPases with guanine nucleotide-exchange factors. *Nat. Rev. Mol. Cell Biol.* 6, 167–180.
11. Bernardis, A., and Settleman, J. (2004). GAP control: regulating the regulators of small GTPases. *Trends Cell Biol.* 14, 377–385.
12. Garcia-Mata, R., Boulter, E., and Burrige, K. (2011). The 'invisible hand': regulation of RHO GTPases by RHOGDIs. *Nat. Rev. Mol. Cell Biol.* 12, 493–504.
13. Adamson, P., Paterson, H.F., and Hall, A. (1992). Intracellular localization of the P21rho proteins. *J. Cell Biol.* 119, 617–627.
14. Lang, P., Gesbert, F., Thiberge, J.M., Troalen, F., Dutartre, H., Chavrier, P., and Bertoglio, J. (1993). Characterization of a monoclonal antibody specific for the Ras-related GTP-binding protein Rho A. *Biochem. Biophys. Res. Commun.* 196, 1522–1528.
15. Takaishi, K., Sasaki, T., Kameyama, T., Tsukita, S., Tsukita, S., and Takai, Y. (1995). Translocation of activated Rho from the cytoplasm to membrane ruffling area, cell-cell adhesion sites and cleavage furrows. *Oncogene* 11, 39–48.
16. Guilluy, C., Swaminathan, V., Garcia-Mata, R., O'Brien, E.T., Superfine, R., and Burrige, K. (2011). The Rho GEFs LARG and GEF-H1 regulate the mechanical response to force on integrins. *Nat. Cell Biol.* 13, 722–727.
17. Greenstein, D. (2005). Control of oocyte meiotic maturation and fertilization. *WormBook Dec 28*, 1–12.
18. McCarter, J., Bartlett, B., Dang, T., and Schedl, T. (1999). On the control of oocyte meiotic maturation and ovulation in *Caenorhabditis elegans*. *Dev. Biol.* 205, 111–128.
19. Kovacevic, I., and Cram, E.J. (2010). FLN-1/filamin is required for maintenance of actin and exit of fertilized oocytes from the spermatheca in *C. elegans*. *Dev. Biol.* 347, 247–257.
20. Wissmann, A., Ingles, J., and Mains, P.E. (1999). The *Caenorhabditis elegans* mel-11 myosin phosphatase regulatory subunit affects tissue contraction in the somatic gonad and the embryonic epidermis and genetically interacts with the Rac signaling pathway. *Dev. Biol.* 209, 111–127.
21. Kovacevic, I., Orozco, J.M., and Cram, E.J. (2013). Filamin and phospholipase C- ϵ are required for calcium signaling in the *Caenorhabditis elegans* spermatheca. *PLoS Genet.* 9, e1003510.
22. Bui, Y.K., and Sternberg, P.W. (2002). *Caenorhabditis elegans* inositol 5-phosphatase homolog negatively regulates inositol 1,4,5-triphosphate signaling in ovulation. *Mol. Biol. Cell* 13, 1641–1651.
23. Clandinin, T.R., DeModena, J.A., and Sternberg, P.W. (1998). Inositol triphosphate mediates a RAS-independent response to LET-23 receptor tyrosine kinase activation in *C. elegans*. *Cell* 92, 523–533.
24. Kariya, K., Bui, Y.K., Gao, X., Sternberg, P.W., and Kataoka, T. (2004). Phospholipase Cepsilon regulates ovulation in *Caenorhabditis elegans*. *Dev. Biol.* 274, 201–210.
25. Vázquez-Manrique, R.P., Nagy, A.I., Legg, J.C., Bales, O.A., Ly, S., and Baylis, H.A. (2008). Phospholipase C-epsilon regulates epidermal morphogenesis in *Caenorhabditis elegans*. *PLoS Genet.* 4, e1000043.
26. Bando, T., Ikeda, T., and Kagawa, H. (2005). The homeoproteins MAB-18 and CEH-14 insulate the dauer collagen gene col-43 from activation by the adjacent promoter of the Spermatheca gene sth-1 in *Caenorhabditis elegans*. *J. Mol. Biol.* 348, 101–112.
27. Tse, Y.C., Werner, M., Longhini, K.M., Labbe, J.C., Goldstein, B., and Glotzer, M. (2012). RhoA activation during polarization and cytokinesis of the early *Caenorhabditis elegans* embryo is differentially dependent on NOP-1 and CYK-4. *Mol. Biol. Cell* 23, 4020–4031.
28. Piekny, A.J., and Mains, P.E. (2002). Rho-binding kinase (LET-502) and myosin phosphatase (MEL-11) regulate cytokinesis in the early *Caenorhabditis elegans* embryo. *J. Cell Sci.* 115, 2271–2282.
29. Marchler-Bauer, A., and Bryant, S.H. (2004). CD-Search: protein domain annotations on the fly. *Nucleic Acids Res.* 32, W327–W331.
30. McDonnell, A.V., Jiang, T., Keating, A.E., and Berger, B. (2006). Paircoil2: improved prediction of coiled coils from sequence. *Bioinformatics* 22, 356–358.
31. Itoh, T., Erdmann, K.S., Roux, A., Habermann, B., Werner, H., and De Camilli, P. (2005). Dynamin and the actin cytoskeleton cooperatively regulate plasma membrane invagination by BAR and F-BAR proteins. *Dev. Cell* 9, 791–804.
32. Tsujita, K., Suetsugu, S., Sasaki, N., Furutani, M., Oikawa, T., and Takenawa, T. (2006). Coordination between the actin cytoskeleton and membrane deformation by a novel membrane tubulation domain of PCH proteins is involved in endocytosis. *J. Cell Biol.* 172, 269–279.
33. Heath, R.J., and Insall, R.H. (2008). F-BAR domains: multifunctional regulators of membrane curvature. *J. Cell Sci.* 121, 1951–1954.
34. Kelley, L.A., and Sternberg, M.J. (2009). Protein structure prediction on the Web: a case study using the Phyre server. *Nat. Protoc.* 4, 363–371.
35. Boratyn, G.M., Schäffer, A.A., Agarwala, R., Altschul, S.F., Lipman, D.J., and Madden, T.L. (2012). Domain enhanced lookup time accelerated BLAST. *Biol. Direct* 7, 12.
36. de Kreuk, B.J., Schaefer, A., Anthony, E.C., Tol, S., Fernandez-Borja, M., Geerts, D., Pool, J., Hambach, L., Goulmy, E., and Hordijk, P.L. (2013). The human minor histocompatibility antigen 1 is a RhoGAP. *PLoS ONE* 8, e73962.
37. Roy, A., Kucukural, A., and Zhang, Y. (2010). I-TASSER: a unified platform for automated protein structure and function prediction. *Nat. Protoc.* 5, 725–738.
38. Zaidel-Bar, R., Joyce, M.J., Lynch, A.M., Witte, K., Audhya, A., and Hardin, J. (2010). The F-BAR domain of SRGP-1 facilitates cell-cell adhesion during *C. elegans* morphogenesis. *J. Cell Biol.* 191, 761–769.
39. Rao, Y., Ma, Q., Vahedi-Faridi, A., Sundborger, A., Pechstein, A., Puchkov, D., Luo, L., Shupliakov, O., Saenger, W., and Haucke, V. (2010). Molecular basis for SH3 domain regulation of F-BAR-mediated membrane deformation. *Proc. Natl. Acad. Sci. USA* 107, 8213–8218.
40. Chiba, Y., and Misawa, M. (2004). The role of RhoA-mediated Ca²⁺ sensitization of bronchial smooth muscle contraction in airway hyper-responsiveness. *Journal of smooth muscle research* 40, 155–167.
41. Fukata, Y., Amano, M., and Kaibuchi, K. (2001). Rho-Rho-kinase pathway in smooth muscle contraction and cytoskeletal reorganization of non-muscle cells. *Trends Pharmacol. Sci.* 22, 32–39.
42. Wing, M.R., Snyder, J.T., Sondek, J., and Harden, T.K. (2003). Direct activation of phospholipase C-epsilon by Rho. *J. Biol. Chem.* 278, 41253–41258.
43. Sukharev, S. (1999). Mechanosensitive channels in bacteria as membrane tension reporters. *FASEB J.* 13, S55–S61.
44. Gauthier, N.C., Masters, T.A., and Sheetz, M.P. (2012). Mechanical feedback between membrane tension and dynamics. *Trends Cell Biol.* 22, 527–535.
45. Keren, K. (2011). Cell motility: the integrating role of the plasma membrane. *Eur. Biophys. J.* 40, 1013–1027.
46. Diz-Muñoz, A., Fletcher, D.A., and Weiner, O.D. (2013). Use the force: membrane tension as an organizer of cell shape and motility. *Trends Cell Biol.* 23, 47–53.
47. Keren, K., Pincus, Z., Allen, G.M., Barnhart, E.L., Marriott, G., Mogilner, A., and Theriot, J.A. (2008). Mechanism of shape determination in motile cells. *Nature* 453, 475–480.
48. Gauthier, N.C., Fardin, M.A., Roca-Cusachs, P., and Sheetz, M.P. (2011). Temporary increase in plasma membrane tension coordinates the activation of exocytosis and contraction during cell spreading. *Proc. Natl. Acad. Sci. USA* 108, 14467–14472.
49. Bigay, J., Gounon, P., Robineau, S., and Antonny, B. (2003). Lipid packing sensed by ArfGAP1 couples COPI coat disassembly to membrane bilayer curvature. *Nature* 426, 563–566.
50. Timmons, L. (2006). Delivery methods for RNA interference in *C. elegans*. *Methods Mol. Biol.* 357, 119–125.
51. Marchler-Bauer, A., Lu, S., Anderson, J.B., Chitsaz, F., Derbyshire, M.K., DeWeese-Scott, C., Fong, J.H., Geer, L.Y., Geer, R.C., Gonzales, N.R., et al. (2011). CDD: a Conserved Domain Database for the functional annotation of proteins. *Nucleic Acids Res.* 39, D225–D229.
52. Notredame, C., Higgins, D.G., and Heringa, J. (2000). T-Coffee: A novel method for fast and accurate multiple sequence alignment. *J. Mol. Biol.* 302, 205–217.
53. Waterhouse, A.M., Procter, J.B., Martin, D.M., Clamp, M., and Barton, G.J. (2009). Jalview Version 2—a multiple sequence alignment editor and analysis workbench. *Bioinformatics* 25, 1189–1191.
54. Biegert, A., Mayer, C., Remmert, M., Söding, J., and Lupas, A.N. (2006). The MPI Bioinformatics Toolkit for protein sequence analysis. *Nucleic Acids Res.* 34, W335–W339.
55. Huson, D.H., and Scornavacca, C. (2012). Dendroscope 3: an interactive tool for rooted phylogenetic trees and networks. *Syst. Biol.* 61, 1061–1067.